Journal of Fluids and Structures (2000) **14,** 1145–1171
doi:10.1006/jfls.2000.0316, available online at http://www.idealibrary.com on IDEAL®

LAUNCH VEHICLE BUFFETING WITH AEROELASTIC COUPLING EFFECTS

K. W. Dotson

Structural Dynamics Department, The Aerospace Corporation, P. O. Box 92957 - M4/909 Los Angeles, CA 90009-2957, U.S.A.

R. L. Baker

Fluid Mechanics Department, The Aerospace Corporation, P. O. Box 92957 - M4/967

AND

B. H. Sako

Structural Dynamics Department, The Aerospace Corporation, P. O. Box 92957 - M4/915

(Received 18 March 1999, and in final form 6 June 2000)

Launch vehicle structural responses can couple with transonic flow state transitions at the nose of payload fairings. This self-sustained coupling yields a nonlinear equation of motion that can be analyzed using the force–response relationship and the periodicity condition. The traditional analysis approach for this phenomenon, however, linearizes the equation of motion by converting the alternating flow forces into an aerodynamic damping term and defines a stability criterion as the response amplitude that yields zero net system damping. This work clarifies the relationship between the present and traditional methods, and compares results and conclusions. The feasibility of modifying a launch vehicle response analysis of buffeting (random pressure fluctuations caused by turbulent flow) to include aeroelastic coupling effects is also explored. The aerodynamic stiffness and damping terms formulated herein are consistent with trends observed in wind-tunnel test data. It is shown, however, that the modified buffet analysis can be inaccurate, particularly when the aeroelastic coupling contribution does not dominate the system response.

1. INTRODUCTION

During transonic flight the flow at the cone cylinder junction of launch vehicle payload fairings can alternate between separated and attached states (Chevalier & Robertson 1963; Robertson & Chevalier 1963). Schlieren photographs from Robertson & Chevalier (1963) are reproduced in Figure 1. A flow state change on the leeward side of the payload fairing model (with a 25° nose cone angle) is evident when the angle of attack equals two degrees. Because the pressure profiles for the separated and attached states are different, the flow state change imposes an exciting force on the launch vehicle. Investigations of self-sustained coupling of this force with launch vehicle elastic responses have been conducted using three different approaches. Computational fluid dynamics has been used in conjunction with structural dynamic models to predict the launch vehicle behavior (Azevedo 1989; Chen & Dotson 1999). This approach is purely analytical but is computationally intensive and limited by the accuracy of the transonic aerodynamic formulation.

0889–9746/00/111145 + 27 $35.00/0

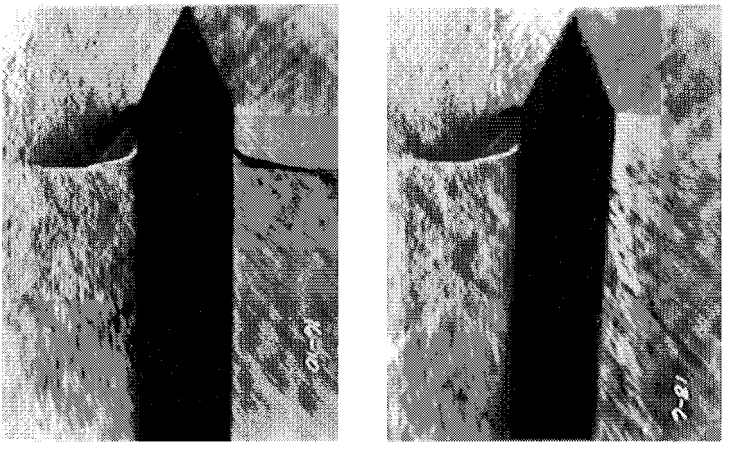

(a) (b)

Figure 1. Schlieren photographs of flow state change observed in wind-tunnel tests for $M_\infty = 0{\cdot}89$: (a) 0° angle of attack; (b) 2° angle of attack. Reproduced with permission of Arnold Engineering Development Center.

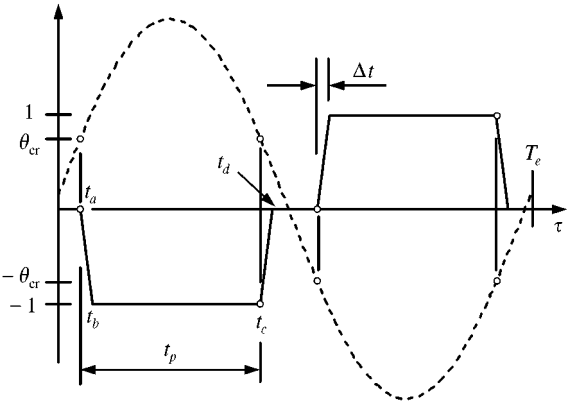

Figure 2. Schematic of one cycle of steady-state coupled force and response in present theory. —, Normalized force variation ξ_a; - - - -, payload fairing rotation.

The other two methods are more tractable for analysis of this phenomenon and use steady experimental data to quantify the pressure distributions on the payload fairing. The unsteady force variation is idealized, and the flow alternations are triggered when the deflection angle reaches a critical value. Ericsson (1967), in the first of these two semiempirical methods, assumed that the flow state changes instantaneously after an implicit time lag and that the alternations occur on only one side of the payload fairing. More recently, Dotson *et al.* (1998a) analyzed the effects of flow state changes that occur linearly during an explicit time lag and on both sides of the payload fairing, as shown in Figure 2. Because most launch vehicles fly with an angle of attack close to zero degrees, and because most payload fairing shapes exhibit flow state alternations for small angle-of-attack values, the two-sided alternations are generally representative of flight conditions. One-sided and instantaneous flow state changes can, however, also be analyzed using the techniques employed by Dotson *et al.* (1998a).

Ericsson (1967) linearized the equation of motion by converting the force from the flow alternations into an aerodynamic damping term corresponding to harmonic response at the vehicle bending mode frequency. A stability criterion was next defined as the limit-cycle amplitude that corresponds to zero net system damping. Dotson *et al.* (1998a), in contrast, established the steady-state behavior of the launch vehicle using analysis techniques for multifrequency periodic excitation. The frequency and amplitude of the limit-cycle oscillations were derived directly, that is, without introducing an aerodynamic damping term.

Self-sustained oscillations for the Titan IV launch vehicle were evaluated by Dotson *et al.* (1998b), and it was shown that the responses and loads can be more than an order of magnitude smaller than those predicted by the Ericsson (1967) stability criterion. It was, furthermore, shown that this difference can be traced to the value of the time lag defined explicitly by Dotson *et al.* (1998a) and implicitly by Ericsson (1967). There are two major implications of this finding: first, the stability criterion concept can be misleading because a finite limit-cycle amplitude always exists for structurally damped launch vehicles; second, it is essential that the estimate of the magnitude of the time lag be reasonable, otherwise the predicted launch vehicle responses and loads will be unrealistically large. This overprediction can have highly undesirable programmatic impacts, such as vehicle redesign and launch "no-go" decisions due to lower thresholds on measured day-of-launch winds.

Even though it is unnecessary to define an aerodynamic damping term to determine the limit-cycle amplitude for launch vehicle aeroelastic coupling, it is common, in a variety of flow-induced vibration problems, to equate self-sustained oscillation with a change in the system damping for one or more of the system modes. For example, the "galloping" of ice-laden cables and the vortex-induced oscillation of stacks are civil engineering problems that have been thus analyzed (Dowell 1995). In aeronautical engineering, the torsional response of wings in transonic flow has been expressed as a reduction in net system damping (Mabey 1989). Indeed, launch vehicle aeroelastic coupling belongs, with transonic wing torsion and aircraft control surface "buzz", in the class of single-degree-of-freedom problems involving feedback between transonic shock-wave motion and structural responses. Experimental and empirical solutions are typically used for these problems because the aerodynamic nonlinearities are significant (Dowell 1995).

Equations of motion presented by Ericsson (1967) imply that launch vehicle responses caused by buffeting (that is, by random pressure fluctuations associated with turbulent flow) can be analyzed using modified bending mode stiffness and damping values that account for aeroelastic coupling effects. Buffet forcing functions have broad-band spectra, and buffeting analyses typically include numerous system modes for accurate response and load predictions. Theoretically, in a modified buffet approach, the stiffness and damping values would be altered for the bending mode speculated to experience aeroelastic coupling, and the response analysis would be conducted for the linear multi-degree-of-freedom system. Application of this methodology does not appear to have been demonstrated for launch vehicle aeroelastic coupling. It is interesting to note, however, that such procedures have been developed for the prediction of bridge flutter including buffeting effects (Dowell 1995).

The feasibility of a modified launch vehicle buffet analysis is investigated herein. Analytical results are provided using Titan IV system parameters. It is shown that a buffet analysis without aeroelastic coupling effects must be conducted prior to calculating the modified stiffness and damping values, and that the bending mode response from a modified buffet analysis can be inaccurate. The derivations of the reduced system damping (and ancillary stiffness effect) nevertheless place launch vehicle aeroelastic coupling within the context of other flow-induced vibration problems.

2. ANALYSIS APPROACH

2.1. Airloads Methodology

The equations of motion for the coupled system are given by

$$[I]\{\ddot{q}(t)\} + [C^*]\{\dot{q}(t)\} + [\omega^2]\{q(t)\} = [\phi]_f^{\mathrm{T}}\{F(t)\}, \tag{1}$$

in which

$$\{x(t)\} = [\phi]\{q(t)\}. \tag{2}$$

Nomenclature is defined in Appendix C.

In a rigorous treatment of the transonic system responses, the vector $\{F(t)\}$ would include time-consistent forces induced by buffeting, wind gusts, control system parameters, static aeroelasticity, and vehicle maneuvering, as well as those caused by aeroelastic coupling (Fleming 1994). However, because it is impossible to predict the amplitudes and phasing of the forces that will occur during the actual flight, a rigorous prelaunch analytical treatment is untenable (Kabe 1998). In practice, equation (1) is broken up into constituent airloads events that are analyzed separately and are treated statistically (Fleming 1994). The mean and dispersed values for each of the dynamic load components are predicted, and total loads are computed using a combination equation that yields values for a specified probability of nonexceedance during flight (Macheske *et al.* 1993). The present analysis is consistent with this practice in that the vector $\{F(t)\}$ includes predictions of external forces induced by aeroelastic coupling and buffeting but neglects those caused by other transonic phenomena.

2.2. Single-mode Aeroelastic Coupling

Computational fluid dynamic analyses (Azevedo 1989; Chen & Dotson 1999) suggest that launch vehicle responses are dominated by coupling with a single (generally the fundamental) system bending mode. Numerical studies conducted by Dotson *et al.* (1998b) also indicate that a single mode is excited by an alternating flow force, unless the frequencies of the higher-order components in its Fourier series expansion are very close to the frequencies of other system modes in the plane of the excitation. Equation (1), therefore, can generally be approximated by the governing differential equation for a single-degree-of-freedom system. This simplification has traditionally been exploited for the analysis of launch vehicle aeroelastic coupling.

However, matrix formulations of aerodynamic stiffness and damping exist for the computation of wind-induced launch vehicle loads (Dotson & Tiwari 1996), and could conceivably be developed for transonic alternating flow forces. In this case, modal coupling, represented by off-diagonal aerodynamic stiffness and damping terms, would be computed and the system response would be composed of numerous modal contributors. However, given the semiempirical nature of the force–response relationship, and the apparent single-degree-of-freedom behavior of launch vehicle aeroelastic coupling, it is believed that this comprehensive matrix formulation is unwarranted.

Extracting from equation (1) the modal equation that best represents the ith system bending mode yields

$$\ddot{q}_{t,i}(t) + 2\zeta_i\omega_i\dot{q}_{t,i}(t) + \omega_i^2 q_{t,i}(t) = \sum_{j=1}^{2} \phi_{i,j}F_{a,j}(q_{t,i}) + \sum_{k=1}^{m} \phi_{i,k}F_{b,k}(t). \tag{3}$$

The ϕ values in equation (3) correspond to the points in the launch vehicle model at which the discrete force histories are applied. The first term on the right-hand side of equation (3)

represents the generalized force history for aeroelastic coupling. The two force resultants in this summation are defined by steady pressure profiles for the alternating flow states, and are described in further detail by Dotson *et al.* (1998a). The alternating flow forces are a function of the generalized displacement $q_{t,i}$, because the changes in flow state occur when the deflection angle of the payload fairing nose cone equals a critical value, as shown in Figure 1.

Dotson *et al.* (1998a) proved, using energy principles, that the generalized aeroelastic coupling force must be out of phase with the vehicle response to induce limit cycle oscillation. For the Titan IV at Mach 0·8, the amplitudes $F_{a,1}$ and $F_{a,2}$ equal 6·7 and 26·2 kN, respectively (Dotson *et al.* 1998a). The corresponding generalized force history is in-phase with the vehicle response; the flow state changes consequently cannot induce limit cycle oscillation for this particular vehicle. Herein, the signs of these force resultants are artificially reversed so that the generalized force history is out of phase with the vehicle response, and Titan IV modal data can be used to analyze buffeting responses with aeroelastic coupling effects. The fundamental pitch bending mode for a Titan IV mission with a 26·2 m long payload fairing was selected for the present study. The frequency and damping of this mode equal 1·27 Hz and 0·71%, respectively.

2.3. Parametric Formulation

The maximum static value of the generalized response from aeroelastic coupling alone is defined by

$$q_{\mathrm{st}} = \omega^{-2}|\phi_1 F_{a,1} + \phi_2 F_{a,2}|, \tag{4}$$

in which the subscript i has been dropped for convenience. The value from equation (4) is not constant during transonic flight because the magnitude and location of the force resultants vary with respect to Mach number. If the maximum value of equation (4) during transonic flight is used, normalization of equation (3) with respect to (4) yields

$$\ddot{z}_t(t) + 2\zeta\omega\,\dot{z}_t(t) + \omega^2 z_t(t) = \omega^2 \xi_t(z_t, t), \tag{5}$$

in which

$$\xi_t(z_t, t) = s\xi_a(z_t) + \xi_b(t). \tag{6}$$

The flow state changes initiate when the response equals

$$z_{\mathrm{cr}} = \theta_{\mathrm{cr}}/|\phi_{r,n}|\, q_{\mathrm{st}}. \tag{7}$$

The range of the scalar s in equation (6) is given by $0 \leq s \leq 1$, such that $s = 0$ corresponds to the absence of flow state changes and $s = 1$ corresponds to the maximum contribution of aeroelastic coupling to the total system response. When buffeting is ignored, equation (5) reduces to the nonlinear equation analyzed by Dotson *et al.* (1998a). The buffeting term $\xi_b(t)$, therefore, acts as noise superimposed on the force variation shown in Figure 2.

The value of s changes as the vehicle flies through the transonic region; it begins with $s = 0$, increases to $s = 1$ at the maximum aeroelastic coupling time, and finally returns to $s = 0$ near Mach 1. The signal-to-noise ratio, therefore, generally increases, then decreases, with respect to Mach number and time. In the example to be presented, maximum aeroelastic coupling occurs around Mach 0·8, in accordance with Titan IV flight data (Dotson *et al.* 1998b).

The Titan IV buffet generalized force during transonic flight is shown in Figure 3(a). Ninety-eight [m in equation (3)] buffet forcing functions with frequency content up to 50 Hz are applied to all components of the Titan IV vehicle. These buffet forces are based on wind

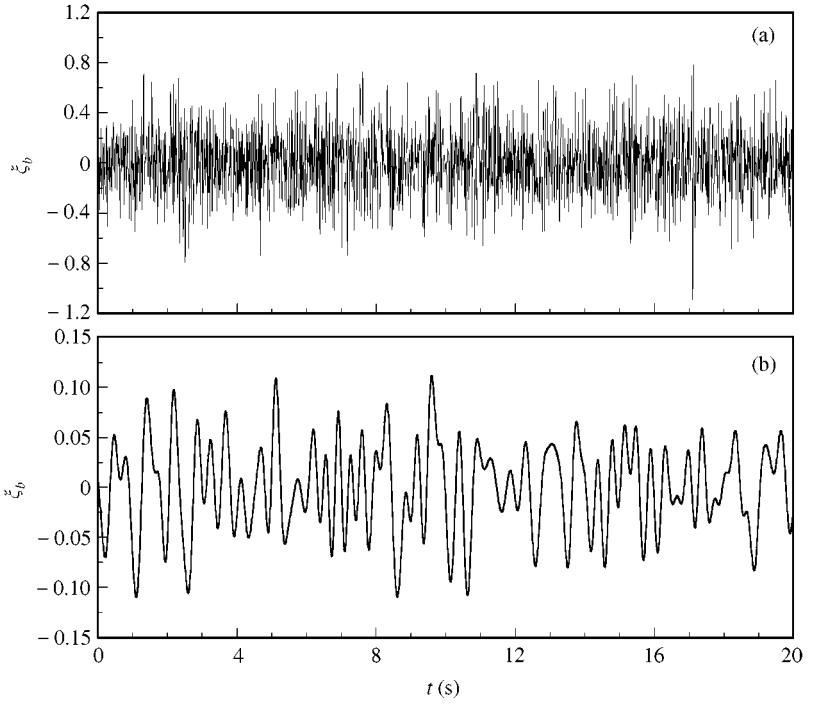

Figure 3. Time history of normalized Titan IV buffet generalized force for fundamental pitch bending mode: (a) 0–50 Hz content; (b) 0–3 Hz content.

tunnel test data but include modifications to ensure conservative response predictions relative to observed flight data. The maximum value of the buffeting noise in Figure 3(a) exceeds unity, the amplitude of the aeroelastic coupling force variation. However, the time history in Figure 3(a) is dominated by frequency components in the 10–20 Hz range and, as shown in Figure 3(b), the amplitude of the content around the frequency of the vehicle fundamental bending mode is relatively low. Indeed, it will be shown that aeroelastic coupling dominates the Titan IV bending response when s is large.

3. AEROELASTIC COUPLING ANALYSIS

Before developing the modified buffet analysis methodology, it is necessary to review solutions for limit-cycle oscillation without buffeting. This section highlights the procedural steps, but also provides analysis conclusions and response comparisons not previously documented.

3.1. Multifrequency Solution

In Dotson *et al.* (1998a) the closed-form solution for the steady-state response of an undamped linear system subjected to the force shown in Figure 2 is used as a trial function for the limit-cycle response from the nonlinear system. The trial function is, therefore, established using the equation of motion

$$\ddot{z}(\tau) + 2\zeta\omega\dot{z}(\tau) + \omega^2 z(\tau) = \omega^2\,\xi(\tau), \qquad 0 \le \tau \le T_e, \tag{8}$$

where ζ is taken to equal zero and the subscript a has been dropped for the sake of clarity. It was shown that the undamped solution accurately predicts the damped response for the ζ-range typical of launch vehicle bending modes. The excitation period T_e is treated as an adjustable parameter, defined by energy principles, once the trial function has been established.

The force variation shown in Figure 2 is antisymmetric about the mid-point of the excitation period. In this case, the steady-state linear response is also antisymmetric such that

$$z(T_e/2 + \tau) = -z(\tau), \qquad 0 \le \tau \le T_e/2, \tag{9a}$$

$$\dot{z}(T_e/2 + \tau) = -\dot{z}(\tau), \qquad 0 \le \tau \le T_e/2. \tag{9b}$$

The solution of equation (8) over each piece-wise-linear force segment in the first half-cycle is given by

$$z(\tau) = C_1 \sin(\omega\tau) + C_2 \cos(\omega\tau), \quad 0 \le \tau \le t_a, \tag{10a}$$

$$z(\tau) = C_3 \sin(\omega\tau) + C_4 \cos(\omega\tau) - (\tau - t_a)/\Delta t, \quad t_a \le \tau \le t_b, \tag{10b}$$

$$z(\tau) = C_5 \sin(\omega\tau) + C_6 \cos(\omega\tau) - 1, \quad t_b \le \tau \le t_c, \tag{10c}$$

$$z(\tau) = C_7 \sin(\omega\tau) + C_8 \cos(\omega\tau) - 1 + (\tau - t_c)/\Delta t, \quad t_c \le \tau \le t_d, \tag{10d}$$

$$z(\tau) = C_9 \sin(\omega\tau) + C_{10} \cos(\omega\tau), \quad t_d \le \tau \le T_e/2. \tag{10e}$$

There are 10 unknown constants in equations (10a)–(10e). Eight of the conditions required to determine the unknowns are established by the continuity of displacements and velocities at the boundaries between the time regions. The remaining two equations are defined by the periodicity requirement and are given by equations (9a) and (9b) with $\tau = 0$. The analytic expressions for these constants are provided in Appendix B.

Finally, in order to satisfy the displacement requirements indicated by the circles in Figure 2, the response from equation (10) is shifted in the direction of the origin by the amount $\Delta t/2$. The trial function is now admissible for the nonlinear equation of motion. It can be shown that the amplitude of the response from equation (10) is defined by

$$\mathrm{AF} = \frac{[\sin(\omega\,\Delta t)/\omega\,\Delta t]\cos(\omega t_a) - [(1 - \cos(\omega\,\Delta t))/\omega\,\Delta t]\sin(\omega t_a)}{\cos(\omega T_e/4)} - 1, \tag{11}$$

where the values t_a and T_e are established below. The response amplitude represents a dynamic amplification factor because the equation of motion was normalized with respect to the static displacement value.

For periodic motion, the work conducted by the alternating flow force must equal the energy dissipated by structural damping during each response cycle. This equality leads to the relationship

$$\int_{z(0)}^{z(T_e)} 2\zeta\omega\dot{z}\,\mathrm{d}z = \omega^2 \int_{z(0)}^{z(T_e)} \xi\,\mathrm{d}z. \tag{12}$$

When $\Delta t \ll T_e$, substitution of equation (10) into (12) yields the characteristic equation

$$\frac{\sin(\omega T_e/2)}{\omega T_e/2} = \frac{1}{1 + \omega\,\Delta t/2\zeta}, \tag{13}$$

from which the period T_e can be computed.

The time point t_a defines the force pulse width t_p and is related to the critical nose rotation for flow state changes. The identity $z_{cr} = z(t_a)$ leads to the analytic expression

$$(2z_{cr} + 1)\cos(\omega T_e/4) = (\omega \Delta t)\sin(\omega T_e/4 - 2\omega t_a) + \cos(\omega T_e/4 - 2\omega t_a), \tag{14}$$

from which the value t_a can be computed.

3.2. Harmonic Approximation

The linear response defined by equation (10) is equivalent to that from Fourier analysis, provided an infinite number of harmonic terms is retained. In other words, application of the method of harmonic balance (Nayfeh & Mook 1979) must converge to the result summarized above as the number of terms increases. Harmonic balance, however, becomes unwieldy in this case, and its use was restricted in Dotson *et al.* (1998a) to a single term. It was shown that the single-term solution (henceforth called the harmonic approximation) is illustrative and sufficiently accurate under certain conditions.

The admissible response function is given by

$$z = \mathrm{AF}\sin(\omega_e(\tau + \Delta t/2)). \tag{15}$$

The fundamental term in the Fourier series expansion of the force variation is given by

$$\xi = -\frac{4}{\pi}\sin(\pi t_p/T_e)\sin(\omega_e \tau), \tag{16}$$

when $\Delta t \ll T_e$. Next, equations (15) and (16) are substituted into equation (8). In accordance with the method of harmonic balance, equating the coefficients of the resulting cosine terms yields

$$\omega T_e/2 = \pi/\sqrt{1 + 4\zeta/\omega \Delta t}. \tag{17}$$

Equation (17) is valid for all critical nose rotation values or, in other words, for all force pulse widths. Equating the coefficients of the sine terms similarly yields

$$\mathrm{AF} = \frac{2f\Delta t}{\zeta}\sin(\pi t_p/T_e). \tag{18}$$

The identity $z_{cr} = z(t_a)$ leads to the analytic expression for the force pulse width of the stable limit-cycle response

$$t_p/T_e = \frac{1}{2} - \frac{1}{2\pi}\sin^{-1}\left(\frac{z_{cr}}{f\Delta t/\zeta}\right). \tag{19}$$

Finally, substituting equation (19) into (18) yields the response amplitude

$$\mathrm{AF} = \frac{f\Delta t}{\zeta}\sqrt{2\left[1 + \sqrt{1 - \left(\frac{z_{cr}}{f\Delta t/\zeta}\right)^2}\right]}. \tag{20}$$

Equation (20) indicates that a limit cycle exists only when $0 \leq z_{cr} \leq f\Delta t/\zeta$. The upper bound of this range is in reasonable agreement with that from the multifrequency solution, and corresponds to an unstable limit cycle. For larger values of z_{cr}, the response spirals in the phase plane to a state of rest.

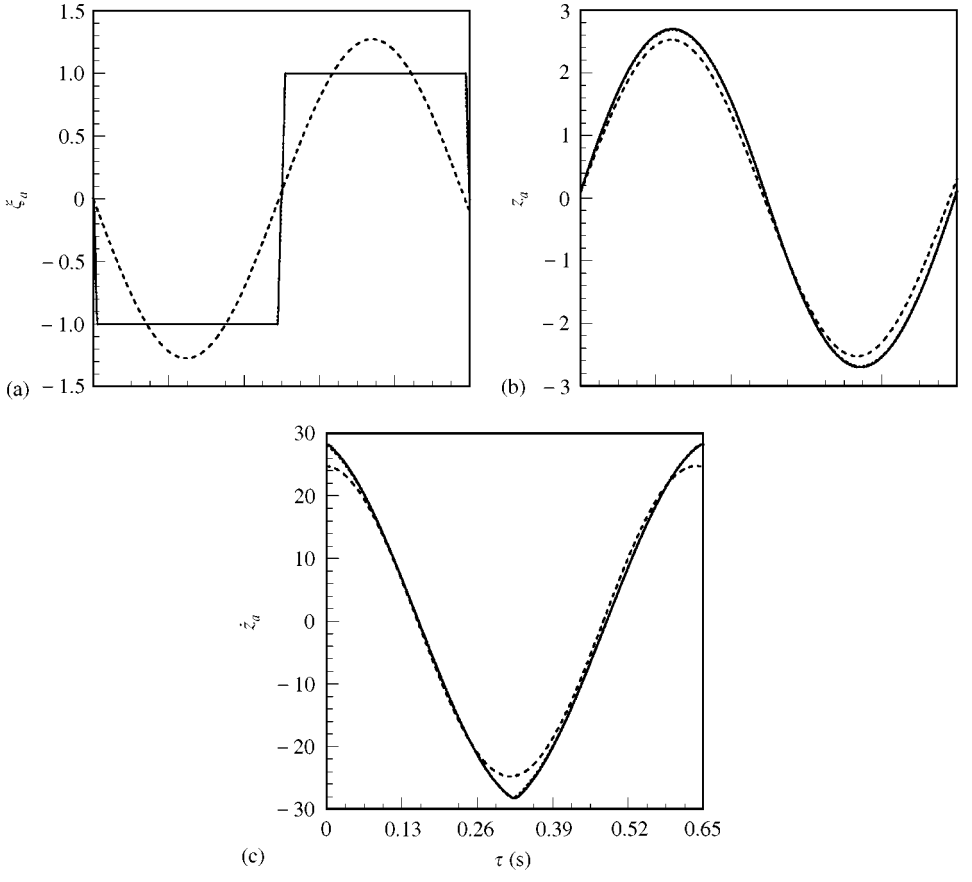

Figure 4. Aeroelastic coupling simulation and analytic histories with $f = 1{\cdot}27$ Hz, $\zeta = 0{\cdot}71\%$, and $\Delta t = 7$ ms: (a) force variation; (b) normalized displacement; (c) normalized velocity. —, Numerical analysis; . . . , multifrequency solution; – – – –, harmonic approximation.

3.3. Response Comparisons

The multifrequency solution and harmonic approximation are compared in Figure 4 with the numerical solution of the nonlinear equation of motion. The Titan IV system parameters were used with a 7 ms time lag, a value supported by Titan IV flight data (Dotson *et al.* 1998b). The critical payload fairing nose cone rotation for the flow state changes was taken as $\pm 0.005^\circ$ ($z_{cr} = 0{\cdot}1$), the value at which the time point t_a vanishes. In this case, the force variation oscillates without dwelling at zero and produces the maximum aeroelastic coupling response. The results from the numerical analysis and the multifrequency solution are virtually indistinguishable, but the displacement and velocity amplitudes for the harmonic approximation are 6·5 and 12% too low, respectively. The harmonic approximation always underestimates the response amplitude; however, its accuracy improves as the salient ratio $f\Delta t/\zeta$ becomes large (Dotson *et al.* 1998a).

3.4. Reduced Frequency

Equation (20) shows that the amplitude of the limit-cycle response varies almost linearly with respect to the time lag Δt. The value of this parameter depends on the mechanisms that

define aeroelastic coupling, and can be expressed as a generalized time lag consisting of components attributable to structural dynamic and aerodynamic effects (Dotson *et al.* 1998b). The structural dynamic component, used implicitly in the traditional formulation (Ericsson 1967), is much larger than that attributable to aerodynamics, but has not been substantiated by flight or wind tunnel test data. Indeed, time lag values extracted from Titan IV flight data are relatively close in magnitude to the aerodynamic component alone (estimated as the distance between the alternating force resultants $F_{a,1}$ and $F_{a,2}$ divided by an approximate flow convection speed).

Dotson *et al.* (1998b) concluded that further work is needed to characterize the nature of the coupling mechanisms and that the time lag should be treated as an explicit analysis variable. It is interesting to note, however, that the concept of reduced frequency k (Dowell 1995) can be introduced if Δt is expressed as L/U_∞, where L is the appropriate length scale for the coupling mechanism. In this case, $k = \omega L/U_\infty$ may be substituted everywhere the product $\omega\Delta t$ appears in the foregoing analytic expressions. [As an example, the frequency and time lag values used herein ($f = 1{\cdot}27$ Hz and $\Delta t = 7$ ms, respectively), yield $k = 0{\cdot}06$, which corresponds to a derived length $L = 1{\cdot}5$ m.] Therefore, all of the derivations, results, and conclusions provided herein may be expressed in terms of reduced frequency, once the mechanisms for launch vehicle aeroelastic coupling have been firmly established.

4. NUMERICAL SIMULATIONS

The buffeting noise plotted in Figure 3(a) is considered to be valid for all transonic Mach numbers, and to be unaffected by local angle-of-attack changes caused by the vehicle bending mode response. The generalized buffeting force, therefore, is treated strictly as a function of time and can be classified as an ideal energy source (Nayfeh & Mook 1979). This approach has traditionally been used by the launch vehicle community for dynamic analysis of launch vehicle loads induced by buffeting.

4.1. Computer Algorithm

The simulation computer algorithm presented by Dotson *et al.* (1998a) was modified to include buffeting noise. The modified code is used herein to assess the effect of buffeting on the aeroelastic coupling response and to validate equations for the effective system frequency and damping. At each time step, the buffeting force ξ_b is added to the aeroelastic coupling force $s\xi_a$ [see equation (6)]. Because buffeting affects the system response, the force variation ξ_a differs from that without buffeting.

The schematic in Figure 2 corresponds to steady-state motion and a linear variation of the aeroelastic coupling force during the time lag Δt. The numerical analysis, on the other hand, includes the transient phase of the response and defines the ramp as a quarter-cycle of a squared sinusoid in the displacement domain. The latter feature eliminates force discontinuities, at the end points of the time lag, that can compromise the stability of the numerical analysis. When the time lag is small with respect to the period of the excitation, the squared sinusoid yields a force variation in the time domain that is, for all practical purposes, linear. The aeroelastic coupling force variation is taken to be out of phase with the response as required for self-sustained oscillation.

Figure 5 shows a schematic of the phase plane diagram, for one response cycle, as implemented in the numerical analysis. The top and bottom parts illustrate the aeroelastic coupling force variation defined by

$$\xi_a = u(z_t) + g(z_t, \operatorname{sgn} \dot{z}_t), \tag{21}$$

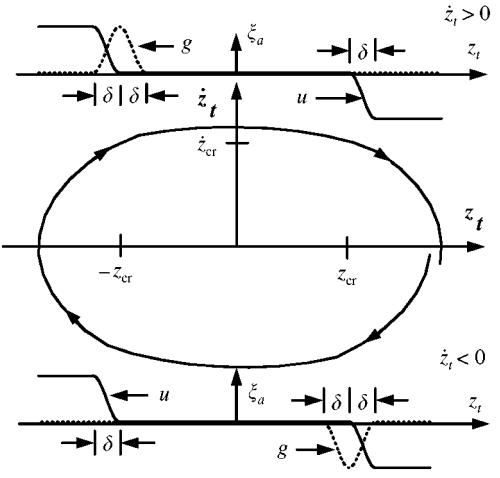

Figure 5. Schematic of phase-plane diagram and transient aeroelastic coupling force variation for one response cycle.

in which

$$u(z_t) = 1, \qquad -z_t - z_{cr} > \delta, \tag{22a}$$

$$u(z_t) = 0, \qquad -z_{cr} < z_t < z_{cr}, \tag{22b}$$

$$u(z_t) = -1, \qquad z_t - z_{cr} > \delta, \tag{22c}$$

$$u(z_t) = \sin^2(\pi(z_t + z_{cr})/2\delta), \qquad 0 \le -z_t - z_{cr} \le \delta, \tag{22d}$$

$$u(z_t) = -\sin^2(\pi(z_t - z_{cr})/2\delta), \qquad 0 \le z_t - z_{cr} \le \delta, \tag{22e}$$

$$g(z_t, \operatorname{sgn}\dot{z}_t) = \cos^2(\pi(z_t + z_{cr})/2\delta), \qquad -\delta \le -z_t - z_{cr} \le \delta, \quad \dot{z}_t > 0, \tag{23a}$$

$$g(z_t, \operatorname{sgn}\dot{z}_t) = -\cos^2(\pi(z_t - z_{cr})/2\delta), \qquad -\delta \le z_t - z_{cr} \le \delta, \quad \dot{z}_t < 0, \tag{23b}$$

$$g(z_t, \operatorname{sgn}\dot{z}_t) = 0, \qquad \text{for all other values of } z_t. \tag{23c}$$

The value of δ is positive and less than z_{cr}, and is chosen such that the aeroelastic coupling force variation exhibits the desired time lag Δt at the limit-cycle state. The computer code solves equation (5), given initial displacement and velocity values. Convergence of the solution is verified by reducing the integration time step and repeating the analysis.

4.2. Numerical Results

Figure 6(a) shows the phase-plane diagram for the Titan IV parameters without buffeting noise. The initial conditions for this simulation are given by zero velocity, and displacement equal to the limit-cycle amplitude, 2·7. Figure 6(b) shows the effect of buffeting noise when $s = 1$, that is, when the aeroelastic coupling contribution is at its maximum. It can be concluded from Figures 6(a) and 6(b) that the inclusion of buffeting noise prevents the system response from attaining a true limit cycle. The aeroelastic coupling contribution, however, is large enough that the deviations from the limit-cycle state are not severe, and the response is quasiperiodic.

Phase-plane diagrams for numerical simulations with the arbitrarily chosen values $s = 0{\cdot}5$ and $0{\cdot}2$ are shown in Figures 6(c) and 6(d), respectively. Because the system displacement is normalized with respect to the maximum aeroelastic contribution, the initial condition $z(0)$ and critical deflection z_{cr} are scaled by s. Figure 6(c) shows that $s < 1$

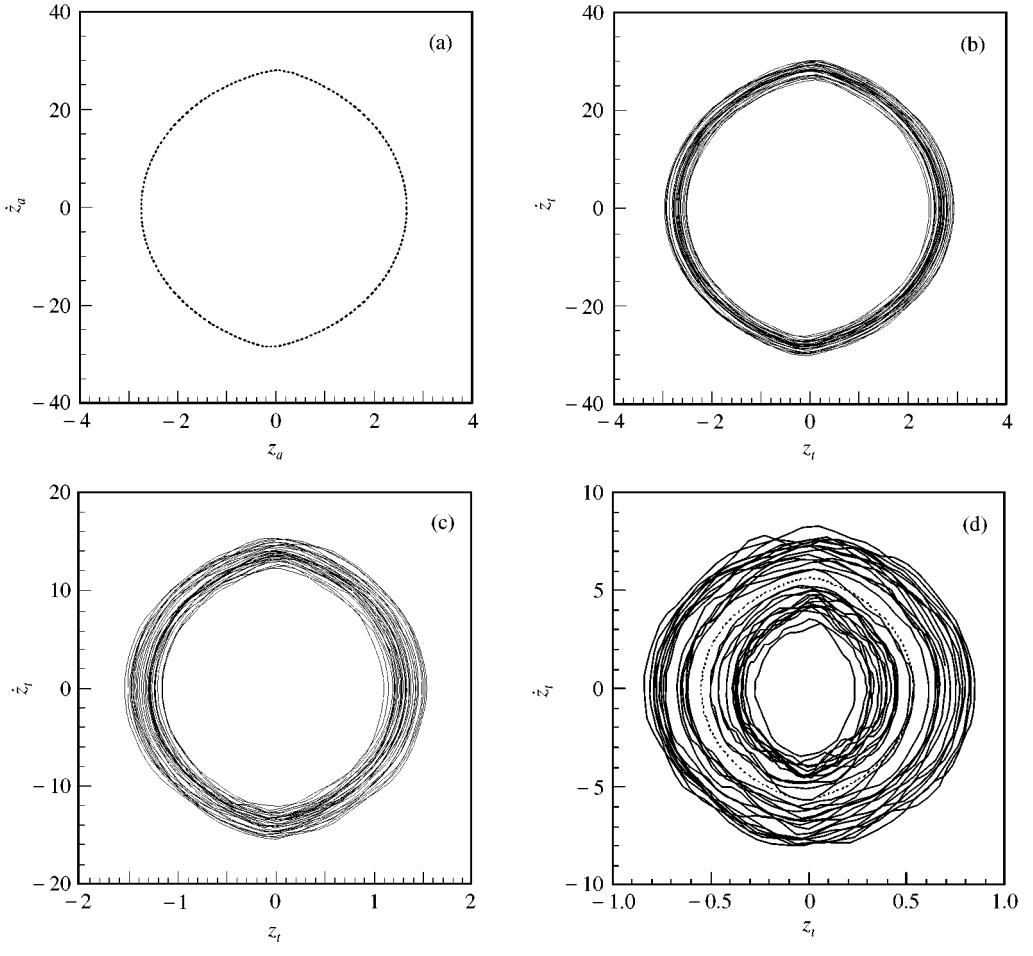

Figure 6. Phase-plane diagram from simulation with $f = 1{\cdot}27$ Hz, $\zeta = 0{\cdot}71\%$, and $\Delta t = 7$ ms: (a) $s = 1$; (b) $s = 1$; (c) $s = 0{\cdot}5$; (d) $s = 0{\cdot}2$. —, With buffeting; - - - -, without buffeting.

increases the relative deviation from the limit-cycle state. Figure 6(d) shows that, when the value of s is small enough, the system response cannot be described as a simple perturbation from that without buffeting.

Force and system displacement histories from the numerical simulation, with $s = 1$, are provided in Figures 7(a) and 7(b), respectively. Histories with and without buffeting noise are shown, as well as the system displacement from buffeting noise alone. These figures further illustrate that, for the Titan IV example, aeroelastic coupling dominates when the signal-to-noise ratio is large.

5. MODIFIED BUFFET ANALYSIS

5.1. Separation of Response Contributions

To assess the effects of buffeting in combination with aeroelastic coupling, equation (5) is split into constituents such that

$$\ddot{z}_a(t) + 2\zeta\omega\,\dot{z}_a(t) + \omega^2 z_a(t) = \omega^2 \xi_a(z_a), \tag{24}$$

$$\ddot{z}_b(t) + 2\zeta\omega\,\dot{z}_b(t) + \omega^2 z_b(t) = \omega^2 \xi_b(t), \tag{25}$$

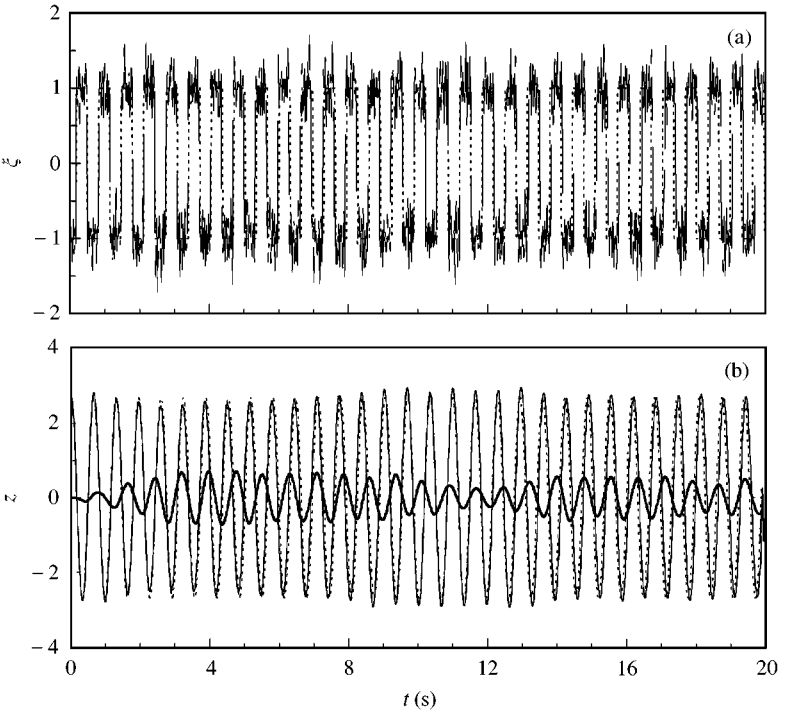

Figure 7. Histories from simulation with $f = 1{\cdot}27$ Hz, $\zeta = 0{\cdot}71\%$, $\Delta t = 7$ ms, and $s = 1$: (a) force variation; (b) normalized displacement. —, With buffeting; - - - -, without buffeting; ——, buffeting only.

in which

$$z_t(t) = sz_a(t) + z_b(t), \quad \dot{z}_t(t) = s\dot{z}_a(t) + \dot{z}_b(t), \tag{26a,b}$$

$$\ddot{z}_t(t) = s\ddot{z}_a(t) + \ddot{z}_b(t) \tag{26c}$$

and the subscript-a terms are defined by aeroelastic coupling without buffeting.

Equation (26) is approximate because response superposition is valid only for linear systems. The approximation is acceptable, however, if the buffeting contribution does not significantly alter the time points at which the system response reaches the critical value for changes in the flow state. In this case, the aeroelastic coupling force variation is close to that without buffeting, as shown in Figure 8(a). Equation (26), therefore, is most useful when the signal strength s is large. As the value of s decreases, the aeroelastic coupling force variation becomes affected by the buffeting response and the accuracy of the approximation diminishes. Figure 8(b) confirms that ξ_a differs significantly from the limit-cycle state when the value of s is small.

5.2. Conversion of Alternating Flow Forces

Conversion of the aeroelastic coupling force variation into equivalent aerodynamic stiffness and damping terms is sought, such that

$$\ddot{z}_a(t) + (2\zeta\omega + \dot{\eta})\dot{z}_a(t) + (\omega^2 + \eta)z_a(t) = 0. \tag{27}$$

Equation (27) can also be expressed as

$$\ddot{z}_a(t) + 2\omega(\zeta + \dot{n})\dot{z}_a(t) + \omega^2(1 + n)z_a(t) = 0. \tag{28}$$

The terms n and $\dot{n}$ modify the system frequency and damping, respectively.

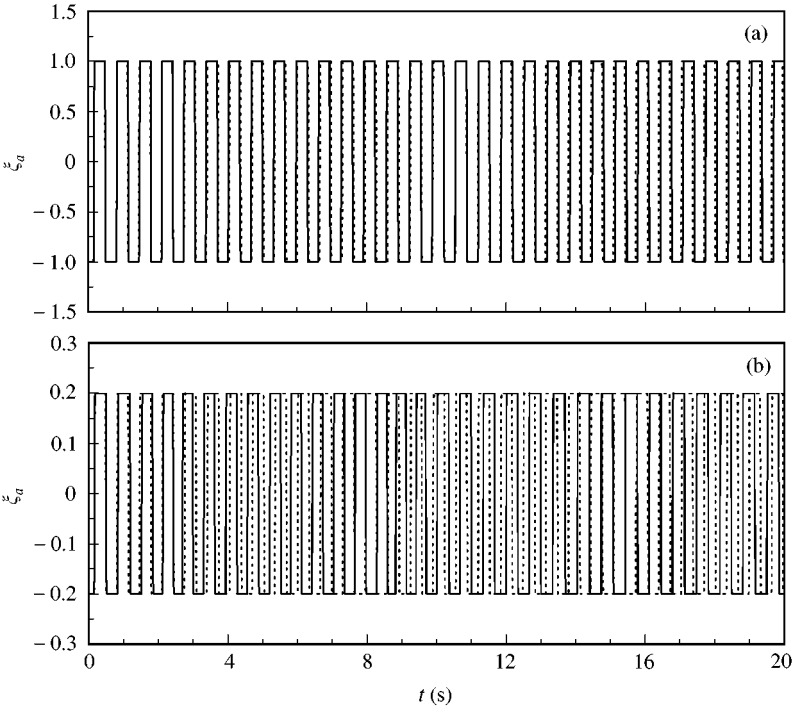

Figure 8. Aeroelastic coupling component of force variation history, from simulation with $f = 1{\cdot}27$ Hz, $\zeta = 0{\cdot}71\%$, and $\Delta t = 7$ ms: (a) $s = 1$; (b) $s = 0{\cdot}2$. —, With buffeting; - - - -, without buffeting.

Equation (28) yields the conventional differential equation for a single-degree-of-freedom linear system:

$$\ddot{z}_a(t) + 2\zeta_a\omega_a\dot{z}_a(t) + \omega_a^2 z_a(t) = 0 \tag{29}$$

when frequency and damping are defined by

$$\omega_a = \omega\sqrt{1+n}, \quad \zeta_a = (\zeta + \dot{n})/\sqrt{1+n}, \tag{30a,b}$$

and the aerodynamic stiffness and damping terms n and $\dot{n}$ are time-invariant.

The aeroelastic coupling response now originates from specified initial conditions because force no longer appears in the equation of motion. The solution of equation (29) is given by

$$z_a(t) = \mathrm{e}^{-\zeta_a\omega_a t}\left[z_a(0)\cos(\bar{\omega}_a t) + \left(\frac{\dot{z}_a(0) + \zeta_a\omega_a z_a(0)}{\bar{\omega}_a}\right)\sin(\bar{\omega}_a t)\right], \tag{31}$$

in which

$$\bar{\omega}_a = \omega_a\sqrt{1-\zeta_a^2}. \tag{32}$$

The exponential in equation (31) can have three effects: if $\zeta_a < 0$, the response grows without bound; if $\zeta_a > 0$, the response tends to rest; and if $\zeta_a \equiv 0$, the response is periodic.

Dotson *et al.* (1998a) used energy principles to prove, and numerical simulations to validate, that when the generalized force caused by the flow state change opposes the bending mode response, and the initial conditions are larger than known critical values, structurally damped systems always attain a stable limit cycle. (The critical initial

conditions in the phase plane are related to the nose rotation for flow state changes, and define an unstable limit cycle.) Only for the unrealistic case in which $\zeta \equiv 0$ will the system response diverge, that is, become unbounded and fail to attain a limiting amplitude. Therefore, effective damping ζ_a ultimately equals zero, which leads to the identity

$$\dot{n} \equiv -\zeta. \tag{33}$$

Dotson *et al.* (1998a) further showed that if the phase-plane coordinates $(z(0), \dot{z}(0))$ lie outside of the stable limit cycle, the transient response diminishes, which implies that the effective system damping is *initially* positive. Similarly, if the phase-plane coordinates $(z(0), \dot{z}(0))$ lie between the stable and unstable limit cycles, the transient response increases, which implies that the effective system damping is *initially* negative. This dependence of the effective system damping value on the initial conditions and time is typical of self-sustained oscillators (Nayfeh & Mook 1979).

A time-invariant value of effective damping ζ_a, therefore, cannot be defined, unless the initial conditions conform exactly to the limit-cycle state. This case is used herein for the modified buffet analysis. Fortunately, the limit-cycle state is of most interest from a response standpoint. That is, if the initial conditions lie outside of the limit cycle, the final response state is more benign than the initial one. Similarly, if the initial conditions lie inside of the limit cycle, the final amplitude is greater and is given by the limit cycle response.

The conversion of periodic flow force alternations into an aerodynamic damping term is constrained by equation (33). It is evident from equation (30a) that the aerodynamic stiffness term is similarly constrained by

$$n \equiv (\omega_a/\omega)^2 - 1 \equiv (fT_e)^{-2} - 1. \tag{34}$$

Figure 9 illustrates equation (34) using T_e values from equation (13). Aerodynamic stiffness n is always positive. Equation (30a) indicates that the effective system frequency is, therefore,

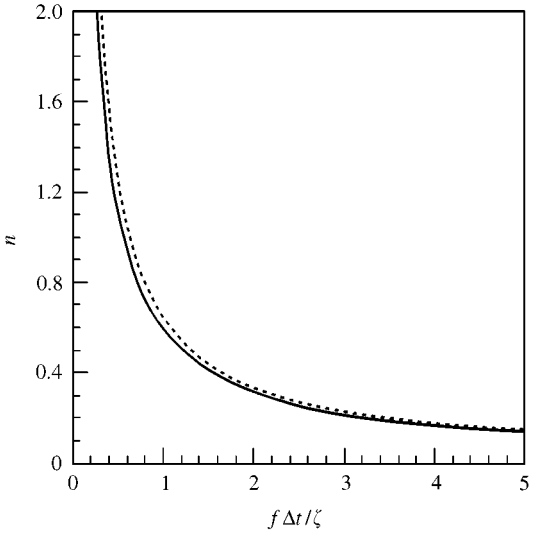

Figure 9. Normalized aerodynamic stiffness: —, multifrequency solution; - - - -, harmonic approximation.

always higher than the natural frequency of the bending mode. This frequency increase is intuitive; the generalized force opposes the system response and, hence, stiffens the system. However, as the salient ratio $f\Delta t/\zeta$ increases, the modification diminishes to zero, and the effective system frequency tends to the natural frequency.

Using equations (17) and (34), it is easy to show that the harmonic approximation yields

$$n = 4\zeta/\omega\Delta t. \tag{35}$$

This expression is compared in Figure 9 with the multifrequency solution. The agreement is reasonable, particularly for the higher values of $f\Delta t/\zeta$.

When $\zeta_a \equiv 0$, equation (29) reduces to

$$\ddot{z}_a(t) + \omega_a^2 z_a(t) = 0, \tag{36}$$

which has a steady-state harmonic as its solution. Hence, the aeroelastic coupling response is harmonic when the step-like forcing function is *implicitly* converted into time-invariant aerodynamic stiffness and damping terms. The force variation ξ_a can instead be *explicitly* moved from the right- to the left-hand side of the equation of motion. This approach, developed in Appendix A, shows that the aerodynamic stiffness and damping terms are time-dependent in a multifrequency formulation.

5.3. Combination of Response Contributions

The equation of motion for the total system response can now be reformulated by summing equations (25) and (36), with the scalar s, such that

$$\ddot{z}_t(t) + 2\zeta\omega\,[\dot{z}_t(t) - s\dot{z}_a(t)] + \omega^2[z_t(t) + nsz_a(t)] = \omega^2\,\xi_b(t). \tag{37}$$

Equation (37) is still unsuitable because it requires aeroelastic coupling displacement and velocity histories. Unless the time dependence of the aeroelastic coupling contribution is removed, there is no benefit in using equation (37), which is approximate, rather than the exact formulation given by equation (5). In other words, time-invariant stiffness and damping coefficients that account for the aeroelastic coupling effects are required if a modified buffet analysis is sought. To this end, a relative measure $\Re$ of the aeroelastic coupling and total responses must be introduced such that

$$\ddot{z}_t(t) + 2\zeta\omega\,[1 - s\Re(\dot{z}_a/\dot{z}_t)]\,\dot{z}_t(t) + \omega^2\,[1 + ns\,\Re(z_a/z_t)]\,z_t(t) = \omega^2\,\xi_b(t). \tag{38}$$

Herein, the value of $\Re$ is established using the root-mean-square (r.m.s.) values of the aeroelastic coupling and buffeting response time histories. In this case, equation (38) yields

$$\ddot{z}_t(t) + 2\zeta\omega\,(1 - s\,\dot{z}_{a,\mathrm{rms}}/\dot{z}_{t,\mathrm{rms}})\,\dot{z}_t(t) + \omega^2(1 + nsz_{a,\mathrm{rms}}/z_{t,\mathrm{rms}})\,z_t(t) = \omega^2\,\xi_b(t). \tag{39}$$

Equation (39) can be written in the conventional form for a single-degree-of-freedom linear system

$$\ddot{z}_t(t) + 2\zeta_t\omega_t\dot{z}_t(t) + \omega_t^2\,z_t(t) = \omega_t^2\,\xi_b'(t), \tag{40}$$

in which

$$\zeta_t = \zeta\left(\frac{1 - s\dot{z}_{a,\mathrm{rms}}/\dot{z}_{t,\mathrm{rms}}}{\sqrt{1 + nsz_{a,\mathrm{rms}}/z_{t,\mathrm{rms}}}}\right), \quad \omega_t = \omega\,\sqrt{1 + nsz_{a,\mathrm{rms}}/z_{t,\mathrm{rms}}}, \tag{41a,b}$$

$$\xi_b'(t) = \frac{\xi_b(t)}{1 + nsz_{a,\mathrm{rms}}/z_{t,\mathrm{rms}}}. \tag{41c}$$

Recall that buffeting noise is considered an ideal energy source and, hence, strictly a function of time. In this case, the aeroelastic coupling and buffeting responses are uncorrelated and the r.m.s. value of the total response can be approximated by

$$z_{t,\mathrm{rms}} = \sqrt{(sz_{a,\mathrm{rms}})^2 + z_{b,\mathrm{rms}}^2}, \quad \dot{z}_{t,\mathrm{rms}} = \sqrt{(s\dot{z}_{a,\mathrm{rms}})^2 + \dot{z}_{b,\mathrm{rms}}^2}. \tag{42a,b}$$

Aeroelastic coupling modifies the system frequency and damping, but the solution of equation (40) nevertheless fails to account for the limit-cycle oscillations, unless appropriate initial conditions such as

$$z_t(0) = \mathrm{AF}, \qquad \dot{z}_t(0) = 0 \tag{43a,b}$$

are specified.

In order to implement equation (40), it is necessary to: (i) define r.m.s. values of the steady-state aeroelastic coupling displacement and velocity; (ii) conduct a transient buffeting analysis without aeroelastic coupling effects; (iii) compute the r.m.s. value of the buffeting displacement and velocity; (iv) calculate the stiffness, damping, and force modifications using equation (41); and finally, (v) repeat the transient buffeting analysis with the modified parameters.

Several features of equation (40) should be noted. First, as the aeroelastic coupling response diminishes, equation (40) reduces to equation (25); similarly, as the buffeting force tends to zero, equation (40) reduces to equation (36). Second, the effective damping value, defined by equation (41a), is nonnegative and has the range $0 \leq \zeta_t \leq \zeta$. Third, as a consequence, the aeroelastic coupling component, introduced through the initial conditions, generally decreases over the analysis duration. And finally, the value of s first increases, then decreases, as the launch vehicle flies through the transonic region, with the result that the effective frequency and damping values vary with Mach number.

5.4. Example Problem

A modified buffet analysis was conducted using the Titan IV parameters. The closed-form equations for the multifrequency solution indicate that $\mathrm{AF} = 2{\cdot}7$, $z_{a,\mathrm{rms}} = 1{\cdot}9$, and

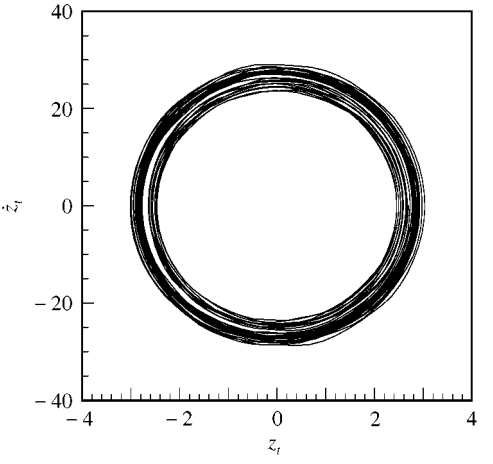

Figure 10. Phase-plane diagram from modified buffet analysis with $f = 1{\cdot}27$ Hz, $\zeta = 0{\cdot}71\%$, $\Delta t = 7$ ms, and $s = 1$.

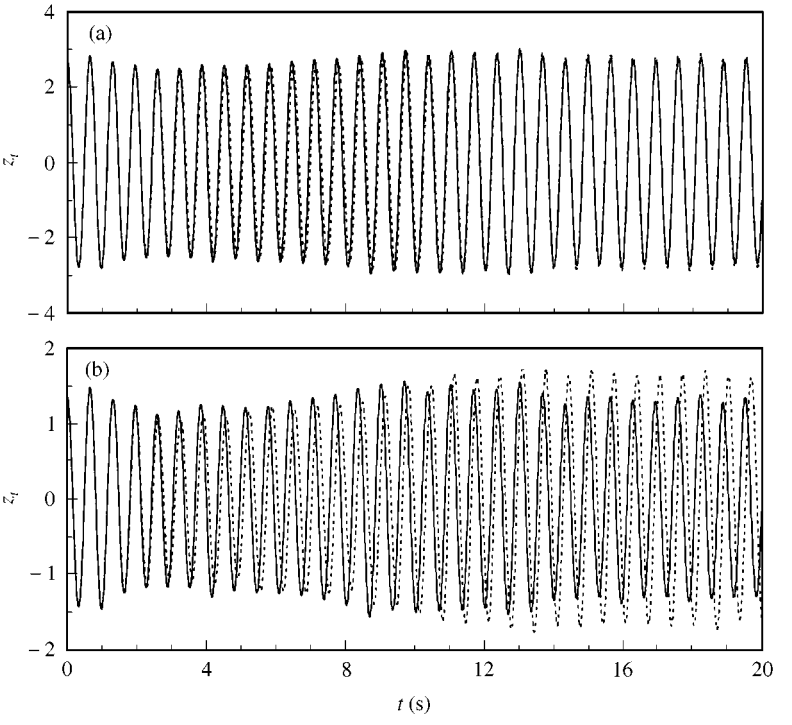

Figure 11. Displacement history with $f = 1{\cdot}27$ Hz, $\zeta = 0{\cdot}71\%$, and $\Delta t = 7$ ms: (a) $s = 1$; (b) $s = 0{\cdot}5$. —, Simulation; - - - -, modified buffet analysis.

$\dot{z}_{a,\mathrm{rms}} = 18{\cdot}7\ \mathrm{s}^{-1}$ for limit-cycle oscillation without buffeting noise (cf. Figure 4). A transient buffeting analysis, without aeroelastic coupling effects and with zero initial conditions, yields $z_{b,\mathrm{rms}} = 0{\cdot}4$ [cf. Figure 7(b)] and $\dot{z}_{b,\mathrm{rms}} = 3{\cdot}0\ \mathrm{s}^{-1}$. Equations (40)–(43), with these response values and $s = 1$, yield the phase-plane diagram shown in Figure 10. This plot should be compared with Figure 6(b), the phase-plane diagram defined by the numerical simulation. The differences, which are most evident at the maximum velocity (force alternation) time points, are caused by the approximations necessary for derivation of equations (40)–(42). Corresponding system displacement histories are plotted in Figure 11(a). The phase and amplitude of the modified buffet response are in reasonable agreement with the numerical simulation when $s = 1$.

The modified buffet analysis was also implemented for the arbitrarily chosen value $s = 0{\cdot}5$. The resulting displacement histories are shown in Figure 11(b). In this case, the methodology initially underpredicts, then, in the last 10 s of the analysis, significantly overpredicts the system response. As the value of s decreases, the aeroelastic coupling force variation becomes influenced by buffeting (see Figure 8), which compromises the periodicity assumed in estimating the aeroelastic coupling contribution to the total system response.

5.5. General Assessment of Aeroelastic Coupling Effects

Trends in effective system frequency and damping are best illustrated using the harmonic approximation of the aeroelastic coupling response, which was defined

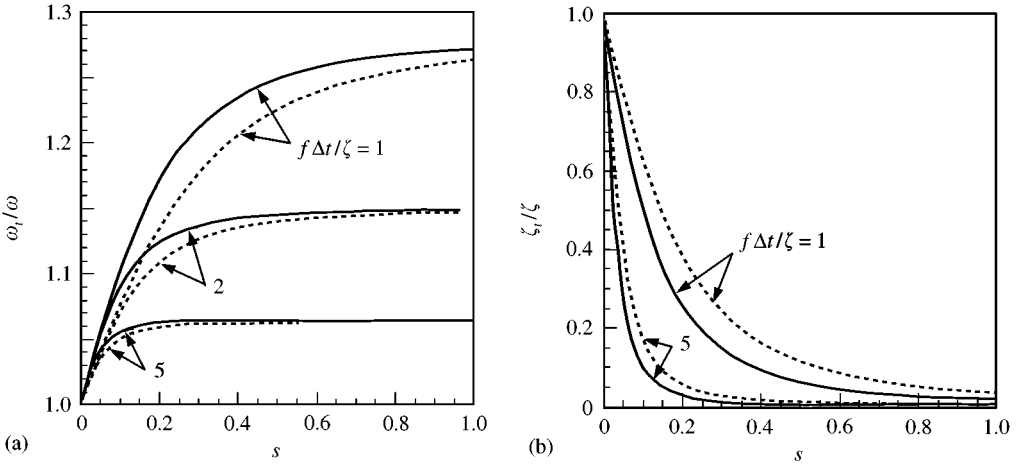

Figure 12. Aeroelastic coupling effects as a function of signal strength: (a) system frequency; (b) system damping. —, $z_{cr} = 0$; - - - -, $z_{cr} = f\Delta t/\zeta$.

in Section 3.2. In this case, the aeroelastic coupling r.m.s. values can be expressed in closed form as

$$z_{a,\mathrm{rms}} = (f\Delta t/\zeta)\sqrt{1 + \sqrt{1 - \left(\frac{z_{cr}}{f\Delta t/\zeta}\right)^2}}, \qquad 0 \le z_{cr} \le f\Delta t/\zeta, \tag{44a}$$

$$\dot{z}_{a,\mathrm{rms}} = \omega\sqrt{1 + 4\zeta/\omega\Delta t}\; z_{a,\mathrm{rms}}. \tag{44b}$$

Figure 12(a) shows curves of frequency, as a function of s, constructed using the modified buffet analysis with the Titan IV parameters and the harmonic approximation for aeroelastic coupling. Results for three values of $f\Delta t/\zeta$, and the z_{cr}-range for limit-cycle oscillation, are illustrated. Since the values of ζ and f are known for the Titan IV example (0·71% and 1·27 Hz, respectively), the curves actually reflect variations in the time lag. For example, $f\Delta t/\zeta = 1$ corresponds to $\Delta t = 5{\cdot}5$ ms. Similarly, z_{cr} can be explicitly evaluated, and $z_{cr} = f\Delta t/\zeta = 1$ corresponds to $\theta_{cr} = \pm 0{\cdot}05^\circ$. Figure 12(a) indicates that aeroelastic coupling only modestly increases the effective system frequency, particularly for large values of $f\Delta t/\zeta$. As aeroelastic coupling decreases relative to buffeting (that is, as the value of s decreases), the system frequency tends to the natural frequency of the vehicle bending mode.

Corresponding curves of effective system damping are shown in Figure 12(b). In contrast to the effective system frequency, the effective system damping depends strongly on the aeroelastic coupling signal strength. A modest contribution from aeroelastic coupling (that is, a small value of s) can lead to a significant drop in effective system damping, even for relatively small values of the time lag. Figure 12(a,b), furthermore, shows that increasing the magnitude of the time lag reduces the effect on system frequency, but exacerbates the effect on system damping. Finally, provided aeroelastic coupling occurs (that is, $0 \le z_{cr} \le f\Delta t/\zeta$), the value of the normalized critical rotation has a minor effect on the system frequency and damping, particularly for large values of $f\Delta t/\zeta$.

Dotson *et al.* (1998a) computed force resultants $F_{a,1}$ and $F_{a,2}$ for $M_\infty = 0{\cdot}8$ and 0·9 and the Titan IV payload fairing geometry. The limit-cycle amplitude for Mach 0·8 is larger because the force resultants for Mach 0·9 shift further aft from the payload fairing nose, and the magnitude of their summation decreases. Titan IV flight data (Dotson *et al.* 1998b)

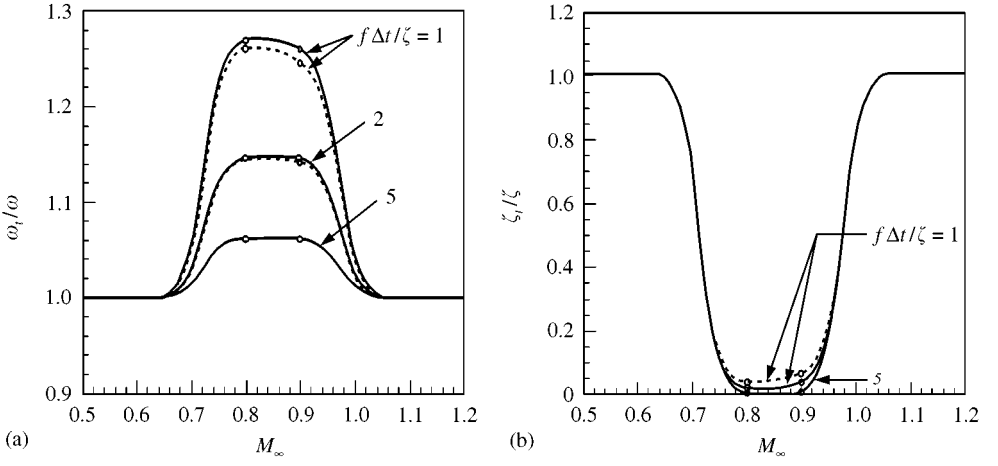

Figure 13. Aeroelastic coupling effects as a function of Mach number: (a) system frequency; (b) system damping. —, $z_{cr} = 0$; - - - -, $z_{cr} = f\Delta t/\zeta$.

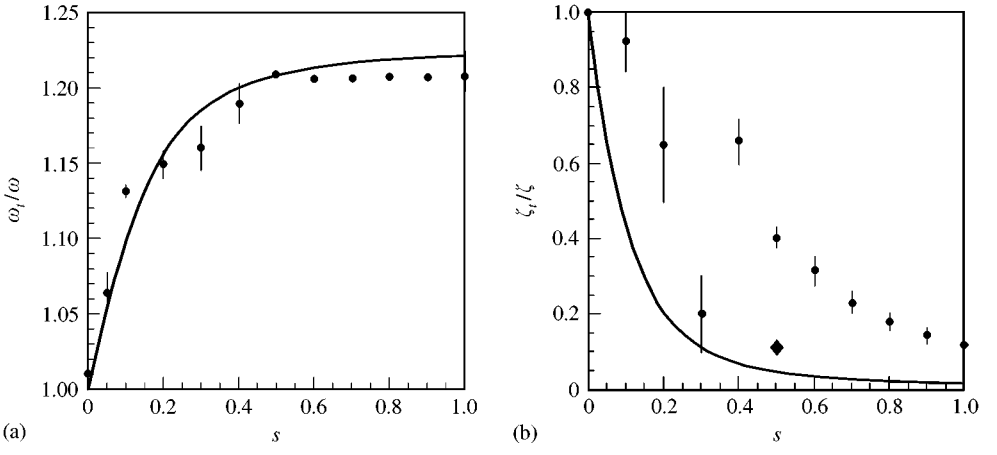

Figure 14. Comparison of analytic and derived estimates: (a) system frequency; (b) system damping. —, Modified buffet analysis; |, range of random decrement estimates; ●, mid-point of range; ◆, trial-and-error value.

suggest that $s = 1$ at roughly $M_\infty = 0{\cdot}8$; in other words, limit-cycle oscillation is maximized around Mach 0·8. It can be shown that the force resultants for $M_\infty = 0{\cdot}9$, in this case, lead to $s = 0{\cdot}7$. Wind-tunnel test data (Chevalier & Robertson 1963; Robertson & Chevalier 1963) also indicate that aeroelastic coupling does not occur when $M_\infty < 0{\cdot}7$ or $M_\infty > 1{\cdot}0$. Using these limits, and the s values described above, the curves in Figure 13 can be sketched.

A "transonic hump" in effective system stiffness is evident in Figure 13(a), while a "transonic dip" in effective system damping is apparent in Figure 13(b). The amplitude of the "transonic hump" is relatively modest, but the minimum of the "transonic dip" approaches zero. The effect of the critical nose deflection (that is, the value of z_{cr}) is secondary. These observations are corroborated by plots of stiffness and damping derived from wind-tunnel test data (Ericsson & Reding 1986).

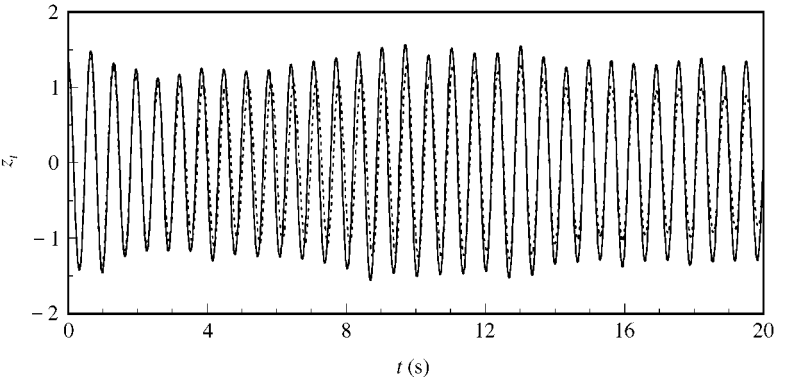

Figure 15. Displacement history from random decrement stiffness and damping estimates: —, simulation; - - - -, random decrement.

5.6. Comparisons with Random Decrement Stiffness and Damping Values

Effective system stiffness and damping values for the Titan IV example are compared in Figure 14 with values derived by applying the random decrement technique (Ibrahim 1977) to the simulation time histories. The random decrement technique averages the random excitation (induced, in this case, by buffeting) out of the total system response, yielding the homogeneous response from which effective system stiffness and damping values can be estimated. The technique has been used for the analysis of flutter data acquired during wind tunnel tests (Hammond & Doggett 1975). The bars in Figure 14 represent uncertainty in the random decrement estimates, and were established by conducting sensitivity studies with the technique's parameters. Random decrement is relatively insensitive to these parameters for large values of s. However, when $0{\cdot}2 \leq s \leq 0{\cdot}4$, the amplitude of the aeroelastic coupling response is roughly equal to that for buffeting, and the random decrement result varies significantly, depending on the parameters chosen.

Figure 14 shows that the trends in the results from the modified buffet analysis and the random decrement technique are similar. The effective system damping from equation (41a), however, is lower than that estimated by the random decrement technique. Because the applied force is known, the accuracy of the random decrement results can be assessed, as were those from the modified buffet analysis (see Figure 11). The single-degree-of-freedom linear response, computed using the random decrement stiffness and damping estimates for $s = 0{\cdot}5$, is compared in Figure 15 with the corresponding numerical simulation response. The random decrement history is in-phase with the simulation, but the response amplitude is significantly underpredicted. Recall that the modified buffet analysis overpredicts the response amplitude for this value of s [Figure 11(b)]. Responses computed by trial-and-error variation of the damping value indicate that $\zeta_t/\zeta = 0{\cdot}11$ yields the best agreement with the simulation response and spectral amplitude, when $s = 0{\cdot}5$. As expected, this value lies between the modified buffet and random decrement estimates in Figure 14(b). It can be concluded that schemes that use time-invariant stiffness and damping values to model nonlinear motion may be heuristic but inaccurate.

6. CONCLUSIONS

The present theory provides straightforward closed-form equations for the prediction of limit-cycle oscillation from aeroelastic coupling, based strictly on the idealized force–response coupling relationship and the periodicity condition. This theory can be used

to derive time-invariant aerodynamic stiffness and damping values in the system equation of motion, and the characteristics of these derived values are consistent with trends observed in transonic wind tunnel test data. The conversion of alternating flow forces into aerodynamic stiffness and damping terms, however, introduces an approximation that tends to underestimate the response amplitude. More important, the use of these terms, in an analysis intended to account comprehensively for aeroelastic coupling and buffeting, must first assess the relative contributions of aeroelastic coupling and buffeting to the total response. When the aeroelastic coupling contribution is large compared to that from buffeting, the modified buffet analysis approach is reasonably accurate. However, discrepancies in response phasing and amplitude can result when the aeroelastic coupling contribution to the total system response is not dominant.

References

Azevedo, J. L. F. 1989 Aeroelastic analysis of launch vehicles in transonic flight. *Journal of Spacecraft and Rockets* **26,** 14–23.

Chen, S.-H. & Dotson, K. W. 1999 A time-marching aeroelastic analysis of launch vehicles in transonic flow. *CEAS/AIAA/ICASE/NASA Langley International Forum on Aeroelasticity and Structural Dynamics.*

Chevalier, H. L. & Robertson, J. E. 1963 *Pressure Fluctuations Resulting from an Alternating Flow Separation and Attachment at Transonic Speeds.* TDR-63-204, Tullahoma, TN, U.S.A.: Arnold Engineering Development Center.

Dotson, K. W. & Tiwari, S. B. 1996 Formulation and analysis of launch vehicle maneuvering loads. *Journal of Spacecraft and Rockets* **33,** 815–821.

Dotson, K. W., Baker, R. L. & Sako, B. H. 1998a Launch vehicle self-sustained oscillation from aeroelastic coupling Part 1: theory. *Journal of Spacecraft and Rockets* **35,** 365–373.

Dotson, K. W., Baker, R. L. & Bywater, R. J. 1998b Launch vehicle self-sustained oscillation from aeroelastic coupling Part 2: analysis. *Journal of Spacecraft and Rockets* **35,** 374–379.

Dowell, E. H. (ed.) 1995 *A Modern Course in Aeroelasticity*, 3rd edition, pp. 119–120, 297–369, 472–532. Dordrecht, The Netherlands: Kluwer.

Ericsson, L. E. 1967 Aeroelastic instability caused by slender payloads. *Journal of Spacecraft and Rockets* **4,** 65–73.

Ericsson, L. E. & Reding, J. P. 1986 Fluid dynamics of unsteady separated flow. Part I. Bodies of revolution. *Progress in Aerospace Sciences* **23,** 1–84.

Fleming, E. R. 1994 Launch vehicle loads. *Flight-Vehicle Materials, Structures, and Dynamics — Assessment and Future Directions. Vol.* 1 — *New and Projected Aeronautical and Space Systems, Design Concepts, and Loads*, A95-24426, pp. 530–541. New York: ASME.

Hammond, C. E. & Doggett, JR. R. V. 1975 Determination of subcritical damping by moving-block/randomdec applications. In *Proceedings of the NASA Symposium on Flutter Testing Techniques*, pp. 59–76, Washington, DC. NASA.

Ibrahim, S. R. 1977 Random decrement technique for modal identification of structures. *Journal of Spacecraft and Rockets* **14,** 696–700.

Kabe, A. M. 1998 Design and verification of launch and space vehicle structures. AIAA Paper 98-1718.

Macheske, V. M., Womack, J. M. & Binkley, J. F. 1993 A statistical technique for combining launch vehicle loads during atmospheric flight. AIAA Paper 93-0755.

Mabey, D. G. 1989 Physical phenomena associated with unsteady transonic flows. *Unsteady Transonic Aerodynamics. Progress in Astronautics and Aeronautics* **120,** 1–55, Washington, DC. AIAA.

Nayfeh, A. H. & Mook, D. T. 1979 *Nonlinear Oscillations*, 1st edition, pp. 59–61, 129–131, 161–224. New York: Wiley & Sons.

Robertson, J. E. & Chevalier, H. L. 1963 *Characteristics of Steady-State Pressures on the Cylindrical Portion of Cone–Cylinder Bodies at Transonic Speeds.* TDR-63-104, Tullahoma, TN, U.S.A.: Arnold Engineering Development Center.

APPENDIX A: INSTANTANEOUS AERODYNAMIC STIFFNESS AND DAMPING

Aerodynamic stiffness and damping expressions were derived in Section 5.2 based on the known behavior of a single-degree-of-freedom system undergoing limit-cycle oscillation from aeroelastic

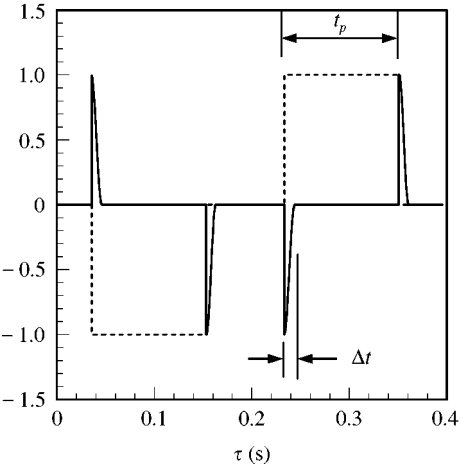

Figure A1. Decomposition of aeroelastic coupling force variation with $f = 2$ Hz, $\zeta = 2\%$, $z_{cr} = 1$, and $\Delta t = 10$ ms: —, ξ_l; - - - -, ξ_p.

coupling. In this section, these expressions are rederived through direct conversion of the force variation ξ_a. (The subscript a is herein dropped for the sake of clarity.) It will be shown that the procedure leads to time-dependent aerodynamic stiffness and damping values, unless the response and force variation are approximated by harmonic functions.

The force variation $\xi(z)$ can be divided into pulses and lags such that

$$\xi(z) = \xi_p(z) + \xi_l(z, \Delta t). \tag{A1}$$

The pulses are the force variation for instantaneous flow alternations, while the lags account for the time that it actually takes the flow state to change. The force components shown in Figure A1 were decomposed from numerical simulation output for an example problem examined by Dotson *et al.* (1998a). It can be seen that the sum of the two force components gives the aeroelastic force variation shown schematically in Figure 2.

The integral of the force variation with respect to displacement z yields

$$\int_{z(0)}^{z(T_e)} \xi \, \mathrm{d}z = \int_0^{T_e} \xi_p \dot{z} \mathrm{d}\tau + \int_0^{T_e} \xi_l \dot{z} \, \mathrm{d}\tau. \tag{A2}$$

The integrands on the right-hand side are illustrated in Figure A2. It is apparent that the first of the two integrals equals zero. It can be concluded from equation (12) that the pulses do not contribute to the net work conducted during one cycle of excitation. This conclusion is consistent with derivations in the displacement domain presented by Dotson *et al.* (1998a), and was confirmed numerically using the data plotted in Figure A2. Equation (12) consequently reduces to

$$\int_{z(0)}^{z(T_e)} 2\zeta\omega\dot{z} \, \mathrm{d}z = \omega^2 \int_{z(0)}^{z(T_e)} \xi_l \, \mathrm{d}z. \tag{A3}$$

Combining the left- and right-hand side yields

$$\int_{z(0)}^{z(T_e)} 2\omega(\zeta + \dot{n})\dot{z} \, \mathrm{d}z = 0, \tag{A4}$$

in which

$$\dot{n} = -\omega\xi_l/2\dot{z}. \tag{A5}$$

Equation (A5) defines the instantaneous aerodynamic damping induced by self-sustained oscillations.

Time histories of the simulation force lags and system velocity are provided in Figure A3. Both of these functions are very nearly even. The result of equation (A5) using these inputs is plotted in Figure A4, and equals zero except for negative spikes coincident with the force lags. Effective system damping, defined by equation (30b), therefore, is actually time-dependent. It can be concluded that it is

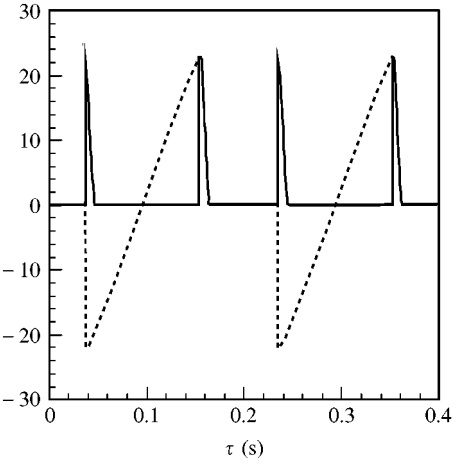

Figure A2. Integrands for work conducted by force variation: —, $\xi_l \dot{z}$; - - - -, $\xi_p \dot{z}$.

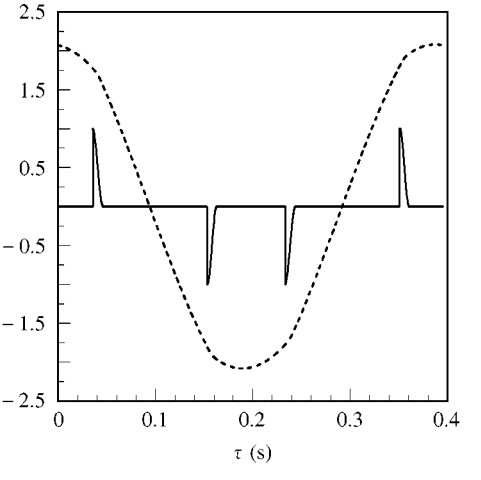

Figure A3. Force lag and system velocity histories: —, ξ_l; - - - -, $\dot{z}/\omega$.

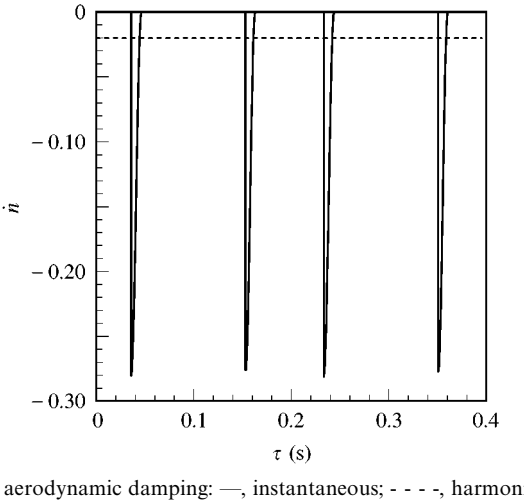

Figure A4. Analytic aerodynamic damping: —, instantaneous; - - - -, harmonic approximation.

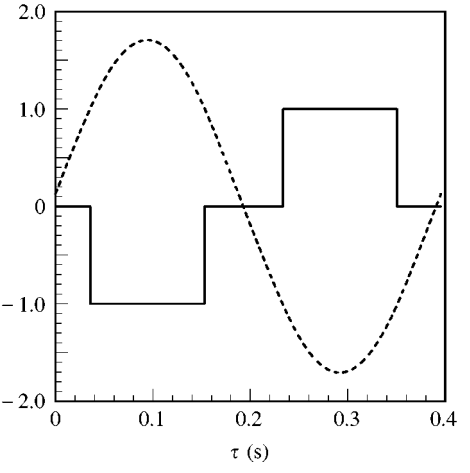

Figure A5. Force pulse and system displacement histories: —, ξ_p; - - - -, z.

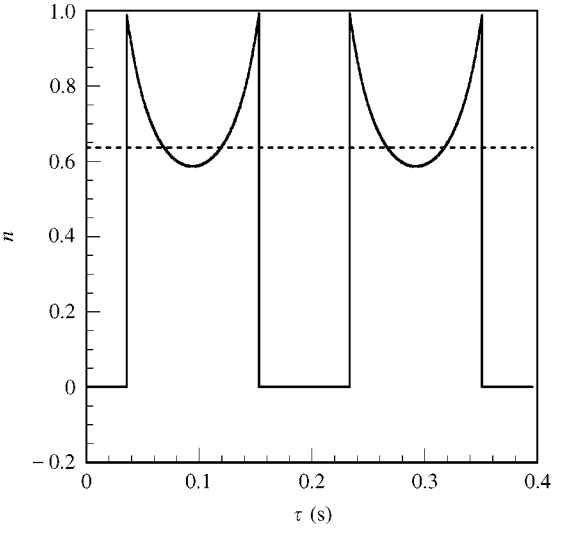

Figure A6. Analytic aerodynamic stiffness: —, instantaneous; - - - -, harmonic approximation.

ad hoc to require, as done in Section 5.2, that the aerodynamic damping be constant and equal to the negative of the structural damping.

When $\Delta t \ll T_e$, the first term in the Fourier series expansion of the force lags is defined by

$$\xi_1(\tau) = \frac{4\Delta t}{T_e} \sin(\pi t_p/T_e) \cos(\omega_e(\tau + \Delta t/2)). \tag{A6}$$

Recall that the harmonic approximation for the response is defined by

$$z(\tau) = \frac{2f\Delta t}{\zeta} \sin(\pi t_p/T_e) \sin(\omega_e(\tau + \Delta t/2)). \tag{A7}$$

Substituting equation (A6) and the derivative of equation (A7) into equation (A5) yields

$$\dot{n} = -\zeta, \tag{A8}$$

which is identical to equation (33). Also, note that equation (A8) satisfies equation (A4) by forcing the sum in the parentheses to equal zero for all time. As expected, the harmonic approximation facilitates conversion of the equation of motion into the form of equation (36).

Now consider the aerodynamic stiffness term. Equation (8) can be rewritten for limit-cycle oscillation as

$$\ddot{z}(\tau) + 2\zeta\omega\,\dot{z}(\tau) + \omega^2 z(\tau) = \omega^2[\xi_p(z) + \xi_l(z, \Delta t)]. \tag{A9}$$

Moving the force lags to the left-hand side yields

$$\ddot{z}(\tau) + 2\omega(\zeta + \dot{n})\,\dot{z}(\tau) + \omega^2 z(\tau) = \omega^2 \xi_p(z), \tag{A10}$$

in which the aerodynamic damping term is defined by equation (A5).

It was shown that the pulse component of the force variation does not contribute to the net work done on the system and, hence, does not alter the system damping. The pulse time history, furthermore, is defined strictly by the instantaneous system displacement. These observations, and the fact that the frequency for limit-cycle oscillation does not equal the bending mode natural frequency, suggests *a posteriori* that conversion of the pulses modifies the coefficient ω^2. Moving this remaining force component to the left-hand side leads to equation (28), in which

$$n = -\xi_p/z. \tag{A11}$$

Time histories of the simulation force pulses and system displacement are plotted in Figure A5. Both of these functions are very nearly odd. The result of equation (A11) is plotted in Figure A6.

The first term in the Fourier series expansion of the force pulses is defined by

$$\xi_p(\tau) = -\frac{4}{\pi}\sin(\pi t_p/T_e)\sin(\omega_e(\tau + \Delta t/2)). \tag{A12}$$

Substituting equations (A7) and (A12) into (A11) yields

$$n = 4\zeta/\omega\Delta t, \tag{A13}$$

which is identical to equation (35) and, hence, consistent with the harmonic approximation of the system response presented in Section 5.2.

APPENDIX B: CONSTANTS IN MULTIFREQUENCY SOLUTION

The constants that satisfy the displacement, velocity, and periodicity conditions for the multifrequency solution are

$$C_1 = [\tan(\omega T_e/4)(\sin(\omega t_b) - \sin(\omega t_a)) + (\cos(\omega t_b) - \cos(\omega t_a))]/\omega\Delta t, \tag{B1}$$

$$C_2 = 0, \tag{B2}$$

$$C_3 = [\tan(\omega T_e/4)(\sin(\omega t_b) - \sin(\omega t_a)) + \cos(\omega t_b)]/\omega\Delta t, \tag{B3}$$

$$C_4 = -\sin(\omega t_a)/\omega\Delta t, \tag{B4}$$

$$C_5 = [\tan(\omega T_e/4)(\sin(\omega t_b) - \sin(\omega t_a))]/\omega\Delta t, \tag{B5}$$

$$C_6 = [\sin(\omega t_b) - \sin(\omega t_a)]/\omega\Delta t, \tag{B6}$$

$$C_7 = [\tan(\omega T_e/4)(\sin(\omega t_b) - \sin(\omega t_a)) - \cos(\omega T_e/2)\cos(\omega t_b) - \sin(\omega T_e/2)\sin(\omega t_b)]/\omega\Delta t, \tag{B7}$$

$$C_8 = [(1 - \cos(\omega T_e/2))\sin(\omega t_b) - \sin(\omega t_a) + \sin(\omega T_e/2)\cos(\omega t_b)]/\omega\Delta t, \tag{B8}$$

$$C_9 = -\cos(\omega T_e/2)[\tan(\omega T_e/4)(\sin(\omega t_b) - \sin(\omega t_a)) + \cos(\omega t_b) - \cos(\omega t_a)]/\omega\Delta t, \tag{B9}$$

$$C_{10} = [(1 - \cos(\omega T_e/2))(\sin(\omega t_b) - \sin(\omega t_a)) + \sin(\omega T_e/2)(\cos(\omega t_b) - \cos(\omega t_a))]/\omega\Delta t. \tag{B10}$$

APPENDIX C: NOMENCLATURE

AF	dynamic amplification factor, dimensionless
$[C^*]$	system modal damping matrix, N s/m and N s/rad
C_1–C_{10}	constants in multifrequency solution, dimensionless
f	natural frequency of a single-system mode, Hz
F	system external force, N

g	component of function $\xi_a(t)$, dimensionless
$\{F(t)\}$	vector of system external forces, N
$[I]$	system modal mass matrix (identity matrix), kg
M_∞	freestream Mach number, dimensionless
n	normalized aerodynamic stiffness for a single-system mode, dimensionless
$\dot{n}$	normalized aerodynamic damping for a single-system mode, dimensionless
$q(t)$	generalized displacement for a single-system mode, m
$\dot{q}(t)$	generalized velocity for a single-system mode, m/s
$\ddot{q}(t)$	generalized acceleration for a single-system mode, m/s^2
$\{q(t)\}$	vector of system generalized displacements, m and rad
$\{\dot{q}(t)\}$	vector of system generalized velocities, m/s and rad/s
$\{\ddot{q}(t)\}$	vector of system generalized accelerations, m/s^2 and rad/s^2
$\Re$	relative measure of aeroelastic coupling contribution to total response, dimensionless
s	aeroelastic coupling signal strength, dimensionless
t	time (transient motion), s
$t_a - t_d$	time points in idealized force representation, s
t_p	force pulse width, s
T_e	excitation period, s
u	component of function $\xi_a(t)$, dimensionless
U_∞	velocity of external flow, m/s
$\{x(t)\}$	vector of physical system displacements, m and rad
z	generalized translation normalized with respect to a static value, dimensionless
Δt	time required for flow state change, s
δ	displacement parameter, dimensionless
ζ	structural damping (as a ratio to the critical value) for a single-system mode, dimensionless
η	aerodynamic stiffness for a single-system mode, rad^2/s^2
$\dot{\eta}$	aerodynamic damping for a single-system mode, rad/s
θ	rotation, deg
ξ	force variation, dimensionless
τ	time (steady-state motion), s
ϕ	modal value for a single-system mode, 1/kg
$[\phi]$	system modes matrix, dimensionless
ω	undamped circular natural frequency of a single-system mode, rad/s
ω_e	$2\pi/T_e$ = circular frequency of excitation, rad/s
$\bar{\omega}$	damped circular natural frequency of a single-system mode, rad/s
$[\omega^2]$	system modal stiffness matrix, N/m and N/rad

Subscripts

a	aeroelastic coupling
b	buffeting
cr	critical
f	physical force application points
i	bending mode number
l	lag
n	nose
p	pulse
r	rotation
rms	root mean square
st	static
t	total (or effective)